Comparing L- and C-band synthetic aperture radar estimates of sea ice motion over different ice regimes

Stephen E.L. Howell, Alexander S. Komarov, Mohammed Dabboor, Benoit Montpetit, Michael Brady, Randall K. Scharien, Mallik S. Mahmud, Vishnu Nandan, Torsten Geldsetzer, John J. Yackel

2018

Remote Sensing of Environment 204 (2018) 380–391

Contents lists available at ScienceDirect

Remote Sensing of Environment

journal homepage: www.elsevier.com/locate/rse

Comparing L- and C-band synthetic aperture radar estimates of sea ice motion over different ice regimes

Stephen E.L. Howell[a,*], Alexander S. Komarov[b], Mohammed Dabboor[c], Benoit Montpetit[d,e], Michael Brady[a], Randall K. Scharien[f], Mallik S. Mahmud[g], Vishnu Nandan[g], Torsten Geldsetzer[g], John J. Yackel[g]

[a] Climate Research Division, Environment and Climate Change Canada, Toronto, Ontario, Canada
[b] Data Assimilation and Satellite Meteorology Research Section, Environment and Climate Change Canada, Ottawa, Ontario, Canada
[c] Meteorological Research Division, Environment and Climate Change Canada, Montreal, Quebec, Canada
[d] Meteorological Service of Canada, Environment and Climate Change Canada, Ottawa, Ontario, Canada
[e] Landscape Science and Technology Division, Environment and Climate Change Canada, Ottawa, Ontario, Canada
[f] Department of Geography, University of Victoria, Victoria, British Columbia, Canada
[g] Department of Geography, University of Calgary, Calgary, Alberta, Canada

ARTICLE INFO

Keywords:
Sea ice
SAR
Ice motion
RADARSAT
PALSAR
L-band
C-band

ABSTRACT

Estimating sea ice motion from synthetic aperture radar (SAR) imagery at C-band is the most reliable approach because of its high spatial resolution and ever increasing temporal resolution given the multiple current and upcoming SAR platforms. However, there is still uncertainty in SAR derived sea ice motion depending on the ice type and its thermodynamic state. There have been suggestions (mostly theoretical) that use of L-band SAR and its inherent longer wavelength (15–30 cm) and subsequent increased penetration capability could be beneficial for estimating sea ice motion, especially during the melt season. Here, we estimate and analyze sea ice motion for 9 pairs of C- and L-band SAR imagery from RADARSAT-2, PALSAR-1 and PALSAR-2 located in the Canadian Arctic over a variety of sea ice types at different thermodynamic states. Results show that the increased signal penetration of L-band SAR into multi-year ice (MYI) during the melt season facilitates the detection of more motion vectors with stronger cross-correlation coefficients compared to C-band SAR. Over newly formed ice and dry first-year ice, the reduced sensitivity to surface scattering and richer texture from L-band SAR imagery facilitates the detection of more motion vectors with stronger cross-correlation coefficients compared to C-band SAR. Over dry MYI, L-band provided stronger cross-correlation coefficients but C-band detected more motion vectors with a more representative spatial distribution. With Arctic sea ice continuing shift from a multi-year to first-year dominated icescape, coupled with an increasing melt season length, L-band SAR's ability to provide improved sea ice motion estimates during both the melt and freeze-up time periods could prove even more useful in the coming decades.

1. Introduction

The decline of Arctic sea ice extent over the past 30 + years is perhaps the most visible feature of climate change (Comiso, 2012; Stroeve et al., 2012). Arctic sea ice has also experienced a decline in age (Maslanik et al., 2011) and thickness (Kwok and Cunningham, 2015) that together with the decline in extent are associated with an overall lengthening of the Arctic melt season (Stroeve et al., 2014). In addition to the aforementioned thermodynamic changes, dynamic sea ice changes are also apparent over the long term record including increasing trends in sea ice motion and convergence (Rampal et al., 2009; Spreen et al., 2011; Kwok et al., 2013; Olason and Notz, 2014). There have also been changes in the dynamic distribution of sea ice, such as increases in the outflow of Arctic Ocean ice through Nares Strait (Kwok et al., 2010) and the Canadian Arctic Archipelago (Howell et al., 2013) as well as changes in ice advection into and out of the Beaufort Sea (Kwok and Cunningham, 2010; Howell et al., 2016; Petty et al., 2016).

Understanding Arctic sea ice variability and change, especially with respect to sea ice dynamics remains a significant challenge, because large-scale monitoring from satellites is only possible within the limits of the sensor utilized. Indeed, considerable progress has been made using synthetic aperture radar (SAR) satellite imagery for the

* Corresponding author.
E-mail address: Stephen.howell@Canada.ca (S.E.L. Howell).

http://dx.doi.org/10.1016/j.rse.2017.10.017
Received 3 June 2017; Received in revised form 27 September 2017; Accepted 13 October 2017
Available online 18 October 2017

Table 1
Dates and times of images used in sea ice motion comparison. All imagery acquired was in ScanSAR mode at HH polarization.

PALSAR-1	RADARSAT-2
2010-04-05 | 19:44:11 UTC	2010-04-05 | 14:29:53 UTC
2010-04-07 | 19:27:00 UTC	2010-04-07 | 15:11:20 UTC
2010-07-23 | 19:45:11 UTC	2010-07-23 | 14:50:33 UTC
2010-07-25 | 19:28:03 UTC	2010-07-25 | 13:51:47 UTC
2010-09-18 | 18:59:35 UTC	2010-09-18 | 13:48:10 UTC
2010-09-24 | 19:46:38 UTC	2010-09-24 | 14:12:50 UTC

PALSAR-2	RADARSAT-2
2016-06-20 | 21:46:34 UTC	2016-06-20 | 15:21:05 UTC
2016-06-24 | 21:32:39 UTC	2016-06-24 | 01:29:48 UTC
2016-07-14 | 20:21:30 UTC	2016-07-14 | 23:38:37 UTC
2016-07-17 | 19:46:43 UTC	2016-07-17 | 23:51:12 UTC
2016-07-22 | 21:33:00 UTC	2016-07-23 | 02:24:00 UTC
2016-07-23 | 21:53:00 UTC	2016-07-24 | 01:55:00 UTC
2016-08-08 | 06:14:36 UTC	2016-08-08 | 01:18:02 UTC
2016-08-09 | 06:35:28 UTC	2016-08-09 | 00:49:09 UTC
2016-10-13 | 21:12:12UTC	2016-10-14 | 02:03:27 UTC
2016-10-14 | 21:33:05 UTC	2016-10-14 | 15:38:01 UTC
2017-01-07 | 21:53:57 UTC	2017-01-08 | 01:54:50 UTC
2017-01-08 | 22:14:49 UTC	2017-01-09 | 01:25:18 UTC

estimation of sea ice motion (e.g. Kwok et al., 1990; McConnell et al., 1991; Karvonen et al., 2007; Thomas et al., 2008; Komarov and Barber, 2014), but the majority of these estimates have typically been made using C-band spaceborne SAR such as ERS-1/2, Envisat-ASAR, RADARSAT-1/2 or Sentinel-1. SAR imagery is advantageous over passive microwave satellite sensors because of its high spatial resolution (50–100 m compared to 12.5–25 km), but there is still uncertainty in the ice motion estimates during the melt season as identifying sea ice features is more difficult due to the presence of liquid water on the ice surface or in the snowpack.

The availability of L-band SAR imagery from PALSAR-1/2 on board the Japan Aerospace Exploration Agency (JAXA) Advanced Land Observing Satellite (ALOS-1/2) provides a significant opportunity to improve estimates of ice motion during the melt season because of increased penetration of electromagnetic waves into the sea ice, including situations when the surface is wet (Onstott and Gogineni, 1985; Onstott et al., 1987). Improved knowledge of ice motion during the melt season is important operationally, especially with respect to multi-year ice (MYI) due to the significant hazard to transiting ships. Several recent studies have documented observed and projected changes in Arctic shipping activities (e.g. Smith and Stephenson, 2013; Melia et al., 2016; Pizzolato et al., 2016), underscoring the need for optimal ice information during the melt season. Recently, Casey et al. (2016) demonstrated that L-band imagery from PALSAR-1 at HH polarization (horizontal transit and receive) provided improved ice type identification (i.e. seasonal versus multi-year) to C-band imagery from RADARSAT-2 at HH polarization during certain melt season stages. Lehtiranta et al. (2015) found that L-band SAR imagery from PALSAR-1 was more useful for estimating sea ice motion when compared to C-band SAR imagery from RADARSAT-2, but their analysis was only focused over dry seasonal ice in the Baltic Sea. The objective of this analysis is to provide a comprehensive investigation on the utility of L-band SAR for estimating sea ice motion compared to C-band SAR over a range of ice types at different sea ice thermodynamic states.

2. Data

2.1. SAR imagery

The primary datasets used in this analysis were SAR imagery in ScanSAR mode from RADARSAT-2 (50 m spatial resolution), PALSAR-1 (100 m spatial resolution) and PALSAR-2 (25 spatial resolution) acquired in 2010, 2016 and 2017 (Table 1). RADARSAT-2 transmits and receives electromagnetic waves at a frequency of 5.405 GHz (C-band) for HH, VV, HV and VH polarizations. PALSAR-1 and PALSAR-2 transmits and receives electromagnetic wave at a frequency of 1.270 GHz and 1.2575 GHz (L-band), respectively for HH, VV, HV and

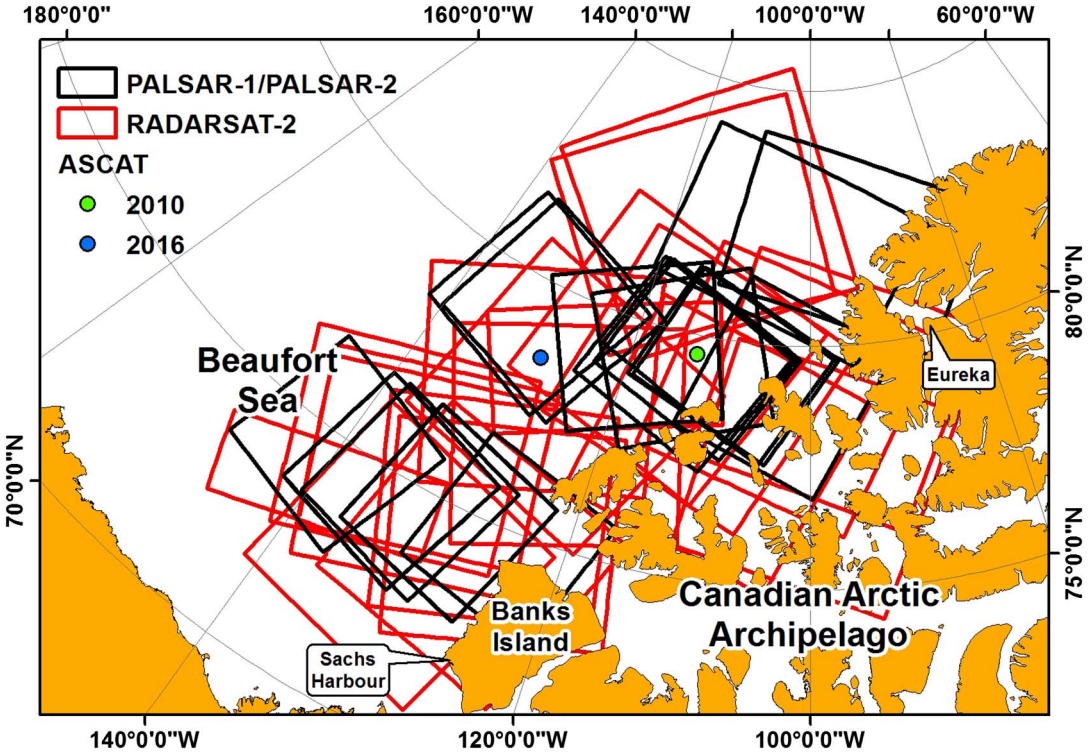

Fig. 1. Locations of the C-band (RADARSAT-2) and L-band (PALSAR-1/PALSAR-2) SAR images used in this analysis. Also shown are the ASCAT pixel locations for 2010 and 2016.

Table 2
Summary table of detected sea ice motion vectors and cross-correlation coefficients for L- and C-band image pairs.

Image dates	Ice type/surface state	L-band			C-band		
		Number of vectors	Mean correlation	Std	Number of vectors	Mean correlation	Std
2010-04-05 | 2010-04-07	MYI/dry	4916	0.482	0.095	6452	0.329	0.083
2010-07-23 | 2010-07-25	MYI/advanced melt	1648	0.184	0.046	1635	0.178	0.045
2010-09-18 | 2010-09-24	MYI/dry	1102	0.278	0.082	2008	0.278	0.088
2016-06-20 | 2016-06-24	MYI/early melt	3402	0.256	0.075	2585	0.192	0.055
2016-07-14 | 2016-07-17	MYI/advanced melt	7835	0.198	0.050	4098	0.182	0.044
2016-07-22 | 2016-07-24	MYI/advanced melt	195	0.226	0.088	111	0.189	0.060
2016-08-08 | 2016-08-09	MYI/advanced melt	5679	0.305	0.087	3724	0.202	0.049
2016-10-13 | 2016-10-14	New ice/freeze up	2971	0.353	0.114	371	0.228	0.075
2017-01-07 | 2017-01-09	FYI/dry	2253	0.484	0.097	1767	0.218	0.058

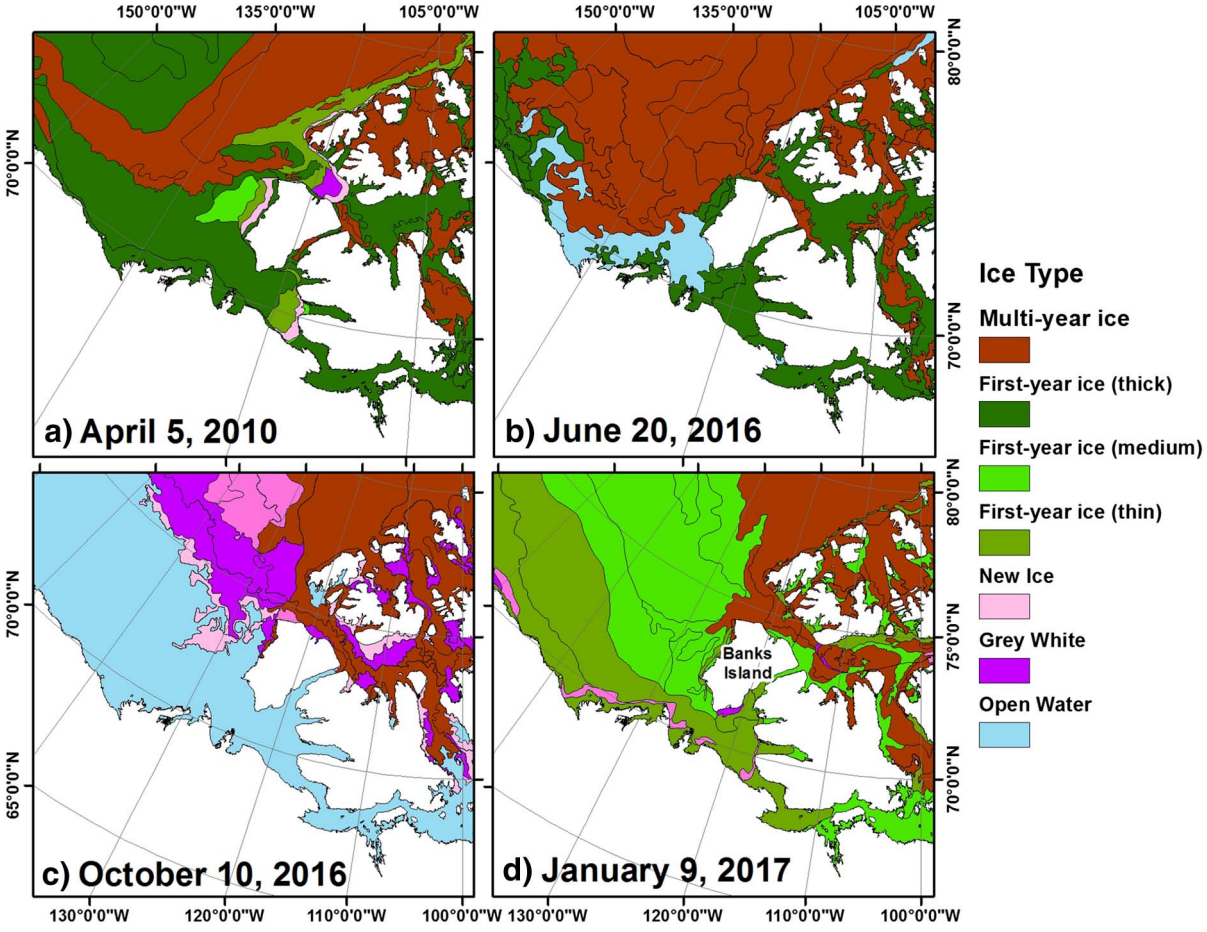

Fig. 2. Canadian Ice Service ice chart classified according to ice type on (a) April 5, 2010, (b) June 20, 2016, (c) October 10, 2016 and (d) January 9, 2017.

VH polarizations. For ScanSAR imagery the available polarization modes of RADARSAT-2 and PALSAR-1/2 are typically HH and HV, or VV and VH. Although some C- and L-band ScanSAR image acquisitions contained an additional HV polarization channel, we chose to use only HH. This was because the HV images from PALSAR-2 appeared to be corrupt, and as a result we decided to omit them since they could not be confidently compared to HV from RADARSAT-2. Moreover, a very low noise floor is required to observe sea ice conditions at HV polarization during the melt season which is problematic for RADARSAT-2 (e.g. Scharien et al., 2014) and currently little information exists for HV scattering from PALSAR-2.

For comparison purposes, our aim was to select images with as little time separation as possible between the RADARSAT-2 and PALSAR-1/2 acquisitions with sufficient spatial overlap. This was a considerable challenge and therefore the time separation was typically within 1-day for most acquisition pairs (Table 1). All image acquisitions where located in the Canadian Arctic, north of the Canadian Arctic Archipelago and the Beaufort Sea (Fig. 1).

2.2. Ancillary datasets

To aid in identifying the ice type and stage of melt in the C- and L-band SAR imagery (see Section 3.2), we used the Advanced Scatterometer (ASCAT) Scatterometer Image Reconstruction (SIR) combined ascending and descending data product at VV polarization from European Space Agency's Meteorological Operational (MetOp) satellite for 2010 and 2016. ASCAT is a real aperture radar operating at 5.255 GHz (C-band). The spatial resolution of ASCAT data is 25 km but the SIR products enhance the spatial resolution to 4.45 km (see Early and Long, 2001 and Lindsley and Long, 2010 for complete details). The ASCAT

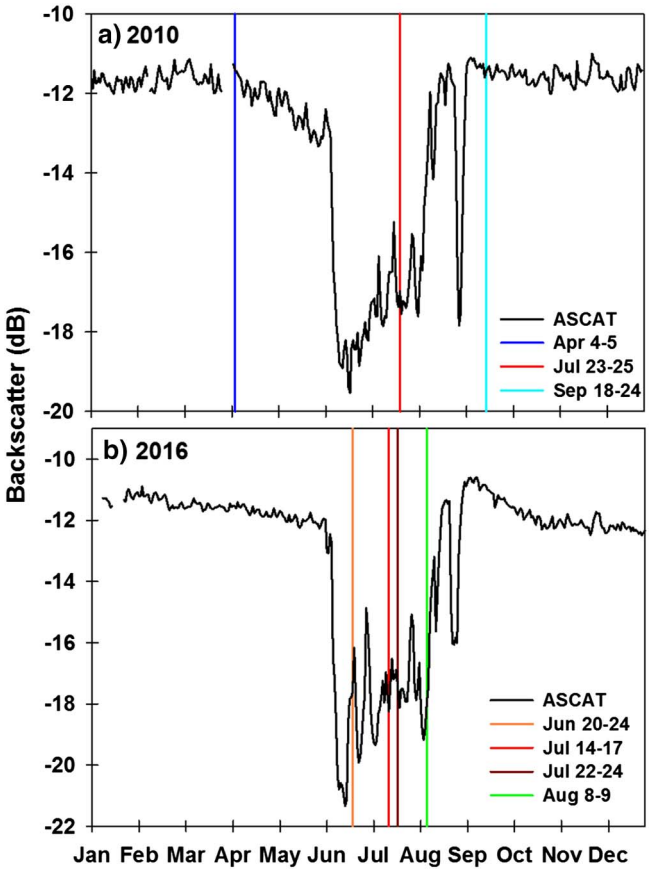

Fig. 3. Time series evolution of the VV-polarized backscatter (dB) from ASCAT for (a) 2010 and (b) 2016. The vertical lines indicate the dates of image pair acquisitions for C- and L-band.

SIR data provide 2-day normalized radar cross-section values at VV polarization with an incidence angle of 40°.

We also used Canadian Ice Service Digital Archive (CISDA) weekly regional ice charts for the closest date to the 2010, 2016 and 2017 image pairs were obtained from the Canadian Ice Service (CIS). CISDA weekly regional ice charts provide information on sea ice area, type and stage of development that integrate all available real-time sea ice information from various satellite sensors (with the primary source being RADARSAT-1 and -2 since 1997), aerial reconnaissance, ship reports, operational model results and the expertise of experienced ice forecasters, spanning 1968 to present (Canadian Ice Service, 2007). In order provide additional context for the stage of melt identification, we use the daily mean air temperatures on the image acquisition dates obtained from Environment and Climate Change (ECCC; http://climate.weather.gc.ca/) weather stations Eureka (79°59′40″N; 85°48′43″W) and Sachs Harbour (71°59′33N; 125°15′15″W) that are in close proximity to the sea ice (Fig. 1).

3. Methods

3.1. Ice motion tracking algorithm

The sea ice motion tracking system used in this study captures both the translational and rotational components of ice motion based on the combination of the phase- and cross-correlation matching techniques with the full details available in Komarov and Barber (2014). Here, only key elements of the ice motion tracking algorithm are outlined, but it has been previously utilized for characterizing 15 + year sea ice motion changes in the Canadian Arctic (e.g. Howell et al., 2013; Howell et al., 2016).

Several spatial resolution levels are generated from the original SAR images (i.e. 100 m in this study) to reduce computational load. At each resolution level a set of control points is automatically generated based on local variances in the SAR image. Thus, various ice features (e.g. cracks and ridges) suitable for tracking are automatically identified. Prior to the ice motion tracking procedure, the Gaussian filter and the Laplace operator are sequentially applied to images at each resolution level in order to highlight the edges and other heterogeneities. The ice tracking algorithm starts with the lowest resolution level to determine preliminary ice motion vectors. To derive ice feature matches, the phase-correlation and cross-correlation techniques are combined. Such an approach makes it possible to find the translational and rotational components of ice motion from the phase-correlation technique as well as to quantitatively estimate the similarity between two sub-images. To eliminate erroneous ice motion vectors, the algorithm compares ice drift vectors derived from the forward pass (tracking from the first image to the second one) and the backward pass (tracking from the second image to the first one). Then additional filtering is performed by thresholding the cross-correlation coefficients. For the rest of the vectors, a confidence level (low, medium, and high) is set up for each output drift vector based on its cross-correlation coefficient. The remaining vectors are further filtered by thresholding their cross-correlation coefficients. At each consecutive resolution level the tracking algorithm run is guided by the ice drift vectors found at the previous resolution level, and thereby, the ice motion field is refined. Both forward and backward passes are conducted at each resolution level to eliminate erroneous vectors. A very good agreement between the SAR derived vectors and ice drifting beacon trajectories located in close proximity to the nearest SAR ice motion vectors was reported in Komarov and Barber (2014). The root-mean square error (RMSE) was 0.43 km for 36 comparison points.

We note that exactly the same algorithm settings were kept throughout all the ice motion tracking runs for both C- and L-band image pairs. No additional image processing was performed on the imagery prior to running the algorithm other than georeferencing and down-scaling the imagery to spatial resolution of 100 m for consistency. We acknowledge that there are well-known limitations of ice motion detection in SAR imagery that include low ice concentration, melt water on the surface and large time duration between image pairs that are applicable to this algorithm (e.g. Wohlleben et al., 2013; Howell et al., 2013; Komarov and Barber, 2014). However, by keeping the time separation between C- and L-band acquisitions as close as possible (i.e. less than 6 h for 14 images and less than 20 h for 4 images; Table 1) these aforementioned factors, other systematic problems (e.g. Hwang, 2013) as well as the drivers of ice speed (e.g. Olason and Notz, 2014) should be more or less equal in both frequency pairs allowing for a robust comparison across different ice regimes. We use the distribution of cross-correlation coefficient values calculated by the algorithm across a SAR image to quantitatively evaluate the quality of ice motion fields derived from C- and L-band SAR images (as described below in Section 4).

3.2. Identifying the ice type and stage of melt

Weekly ice charts from the CISDA were used to identify the ice types for the L- and C-band pairs used in this analysis. While the CISDA provides excellent ice type identification, information on the thermodynamic state of the ice during the melt season is not available. The temporal evolution of the backscatter coefficient (sigma nought; σ°) from active microwave sensors has been widely utilized to estimate the stage of sea ice (e.g. Livingstone et al., 1987; Onstott et al., 1987; Winebrenner et al., 1994; Yackel et al., 2007; Wang et al., 2011; Mortin et al., 2014; Mahmud et al., 2016). This is made possible because over the seasonal cycle of solar insolation, changes in the sea ice thermophysical properties are linked to changes in the dielectric properties and subsequent microwave scattering characteristics. Imagery with high

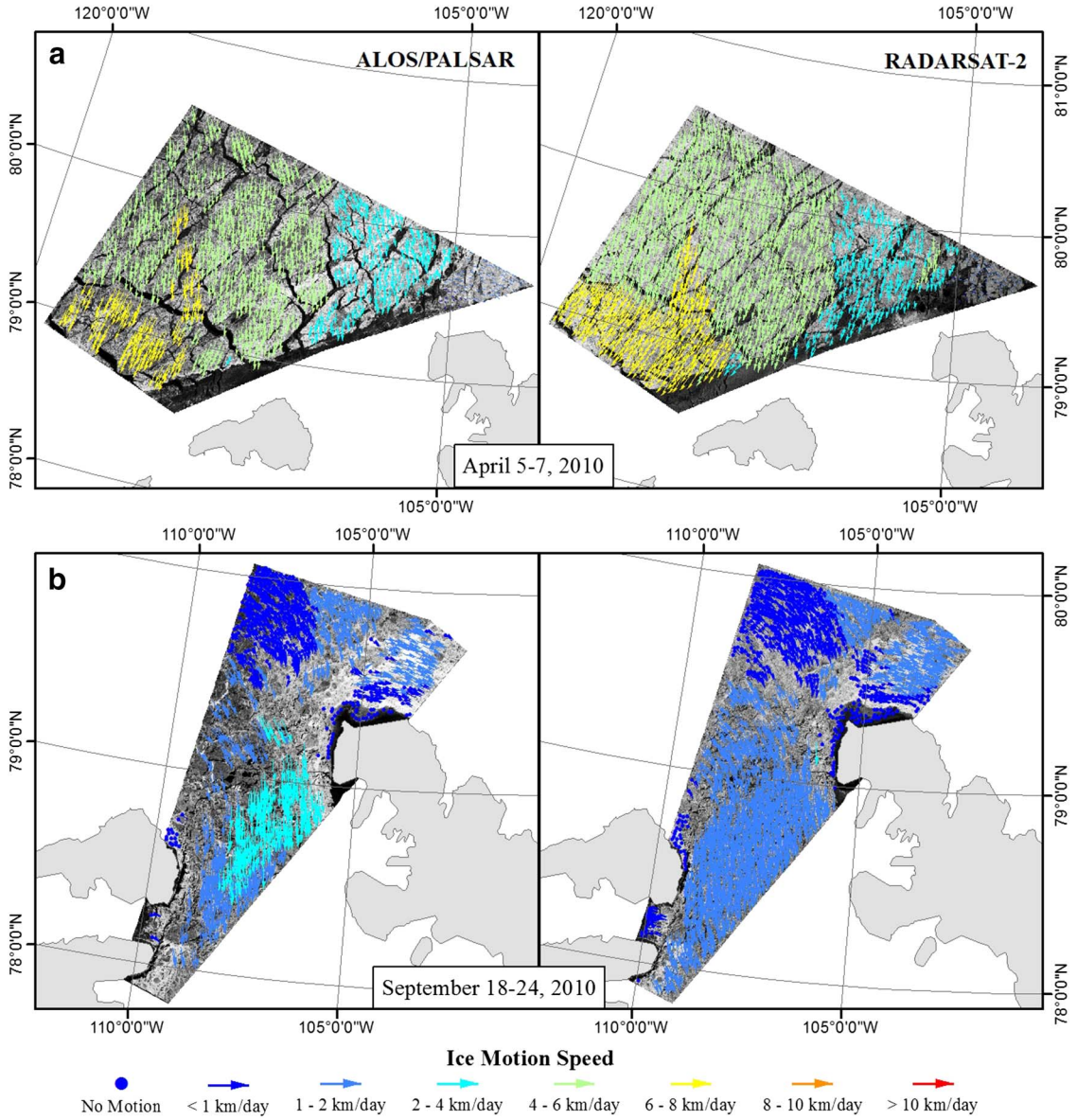

Fig. 4. Spatial distribution of L-band (left) and C-band (right) sea ice motion speeds over dry multi-year ice for (a) April 5–7, 2010 image pairs and (b) September 18–24, 2010 image pairs.

temporal resolution is ideal to identify thermodynamic transitions over sea ice and therefore we make use of the time series evolution of the backscatter from ASCAT (C-band) to identify the thermodynamic state of sea ice for the image pairs used in this analysis (Table 2).

3.2.1. 2010 image pairs

The CISDA weekly chart on April 5, 2010 is shown in Fig. 2a and the time series of ASCAT σ° within or in close proximity to most image pairs in 2010 is shown in Fig. 3a. The region north of the Canadian Arctic Archipelago where the image pairs are located is known to be dominated by MYI throughout the annual cycle (Canadian Ice Service, 2011). Indeed, the CISDA ice chart indicates that MYI was the primary ice type for April 2010 (Fig. 2a) and subsequent CISDA charts confirm that MYI continued to be the primary ice type for the remainder of the year (not shown). Relatively high and stable σ° conditions were present during the April 4–5 image acquisitions which is a result of volume scattering from air bubbles within MYI and is characteristic of dry winter conditions (Fig. 3a). The mean air temperature at the ECCC Eureka weather station from April 5–7, 2010 was −31.4 °C which confirms dry ice conditions were present. At C-band, the first significant downturn in σ° over MYI is an indication of melt onset (i.e. termed early melt). This has been attributed to increases in air temperature and corresponding increases in snow volumetric water content that causes volume scattering from MYI to be attenuated by wet snow layer due to the larger dielectric loss component of the complex permittivity within the wet snow layer (Winebrenner et al., 1994; Barber et al., 1995). In our 2010 study region, Fig. 3a indicates that melt onset occurred in early June.

Following melt onset, σ° over MYI typically increases which is coincident with the ablation of the snow cover and the transition to a high dielectric melt pond surface (e.g. termed advanced melt) after which σ° typically decreases coinciding with the drainage of the melt ponds and a reduction in melt pond fraction (Barber et al., 1995). For the July 23–25 pair, σ° falls during advanced melt and given the fluctuation in σ° it is likely that the ice has reached the melt pond or drainage stage. The mean air temperature at ECCC Eureka weather station for July 23–25, 2010 was 4.3 °C indicating melt was occurring. After the advanced melt stage, σ° over MYI gradually increases as melt ponds freeze and volume scattering within the MYI once again dominates (Beaven and Gogineni, 1994). ASCAT σ° during the September 18–24 image pair acquisition

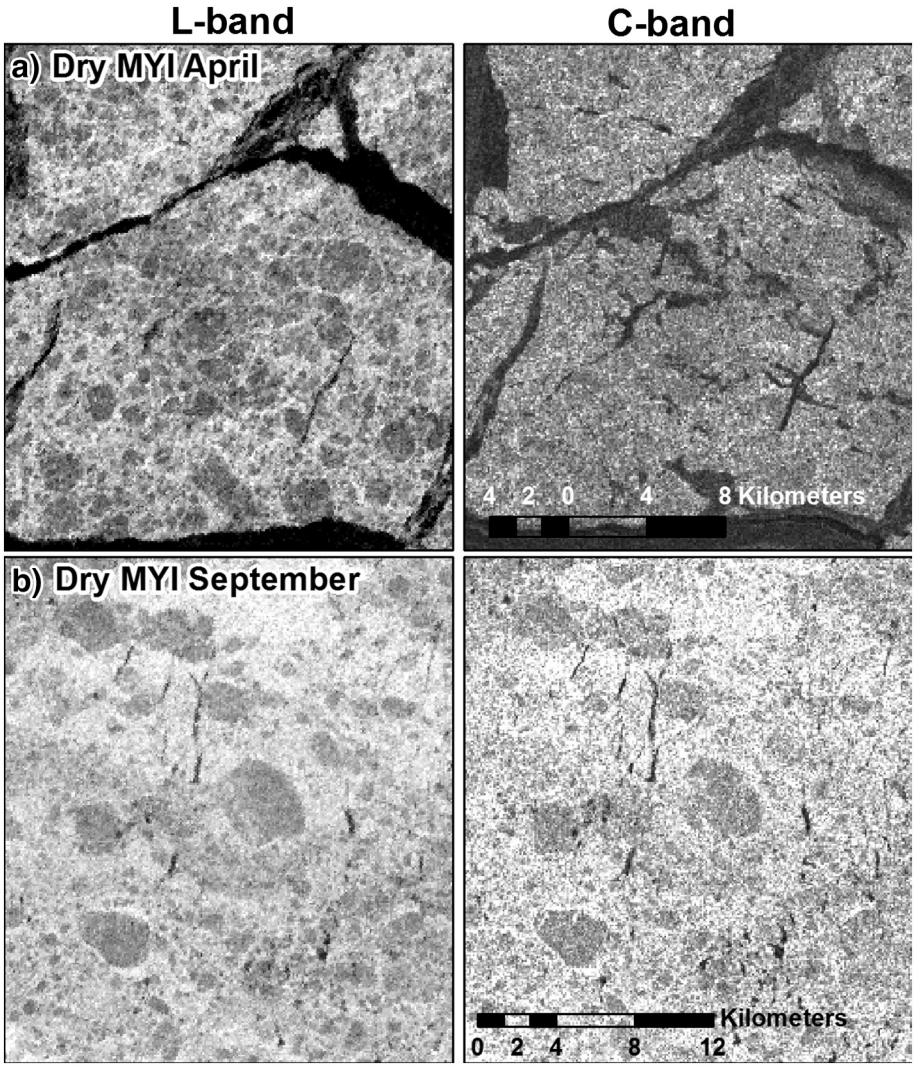

Fig. 5. Magnified images of L- and C-band SAR over (a) dry multi-year ice (MYI) on April 5, 2010 and (b) dry MYI on September 18, 2010.

was high and temporally stable well beyond the freeze-up transition which indicates dry MYI conditions were present that was also confirmed by a mean September 18–24 air temperature at the Eureka ECCC weather station of − 9.8 °C.

3.2.2. 2016 and 2017 image pairs

The CISDA weekly ice chart on June 20, 2016 is shown in Fig. 2b and the corresponding ASCAT σ° time series within or in close proximity the image pairs is shown in Fig. 3b. The June 20–24, July 14–17, July 22–24 and August 8–9 image pairs in 2016 were all over the MYI located in the Canadian Basin north of the Canadian Arctic Archipelago as indicated by the CISDA (only June 20 ice chart is shown). The ASCAT σ° time series suggests that all pairs were acquired during the melt season and mean air temperature at the ECCC Eureka weather station during all image acquisitions were well above 0 °C. The June 20–24 image pair was acquired just following the initial downturn in σ°, therefore the thermodynamic state of the MYI was in the early melt regime. For the remaining image pairs, the ASCAT σ° evolution indicates they were all acquired at the advanced melt stage with the July 14–17 and July 22–24 image pairs likely at the melt pond stage and August 8–9 at the drainage stage.

ASCAT σ° data indicates that freeze up occurred by mid-September (Fig. 3b) but since the remaining pairs were acquired outside of the melt season and we were able to use the CISDA to identify the primary ice type in the imagery. According to the CISDA, the ice conditions for the October 13–14, 2016 image pairs were a mixture of new ice, grey white ice and open water located in the Beaufort Sea (Fig. 2c) and the mean air temperature at Sachs Harbour was − 14.8 °C. For the January 7–9, 2017 image pair, the primary ice type was first-year ice (medium thickness) also located in the Beaufort Sea (Fig. 2d). The mean air temperature at Sachs Harbour from January 7–9, 2017 was − 25.6 °C which indicates dry first-year ice conditions.

4. Results and discussion

4.1. Dry MYI

The spatial distribution of estimated sea ice motion for C- and L-band SAR over dry MYI in early April is shown in Fig. 4a. A more discontinuous spatial distribution is apparent with L-band compared to C-band, with more vectors being detected from C-band compared L-band at 6452 and 4916, respectively (Table 2). Fig. 5a provides a closer examination of dry MYI conditions for these April image pairs at both L- and C-band and it is apparent that ice floes are more easily delineated at L-band. More vectors and the continuous ice motion distribution for C-band occurs because between large MYI floes there is very thin ice to which C-band is more sensitive (Dierking and Busche, 2006; Dierking, 2010), and thus there is texture (rougher) for the tracking algorithm to recognize. At the same time, L-band does not show any image texture between ice floes because ice is very thin and L-band is not sensitive to it as evident with the dark areas between floes in Fig. 5a, therefore producing a less continuous spatial distribution of ice motion compared

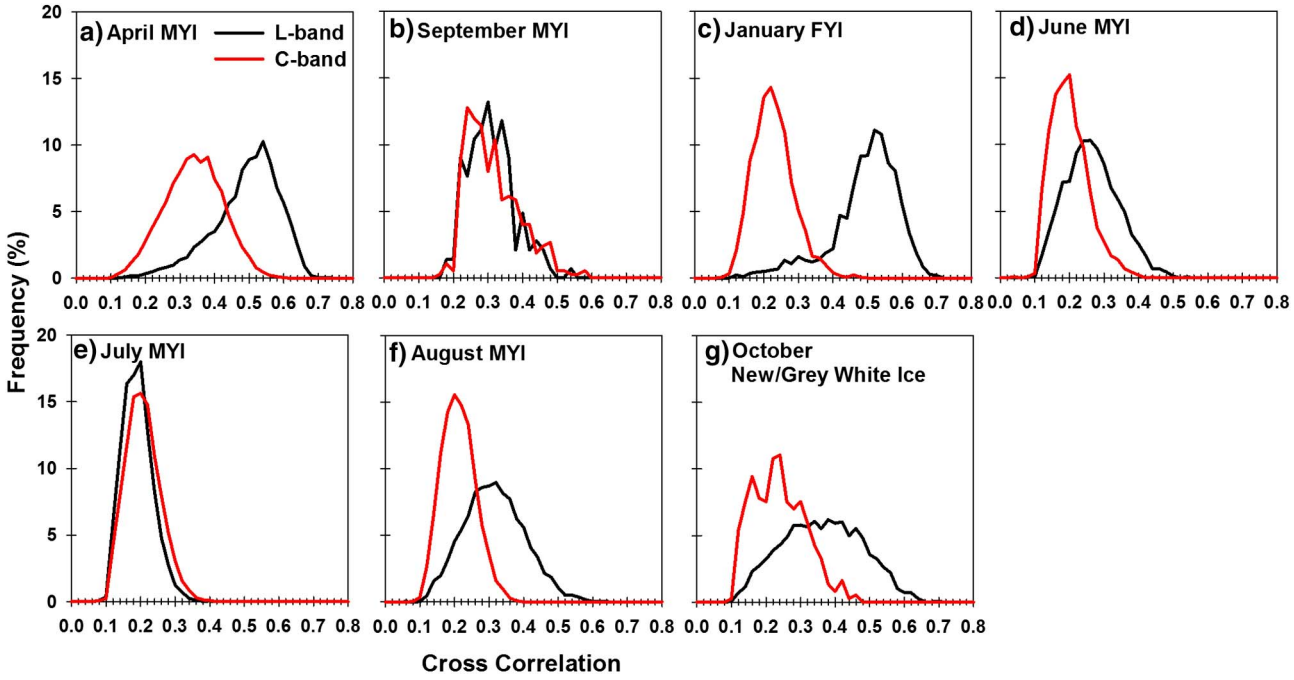

Fig. 6. Frequency distribution (%) of L- and C-band cross-correlation coefficients for (a) April 5–7, 2010 (b) September 18–24, 2010, (c) January 7–9, 2017, (d) June 20–24, 2016 (e) July 14–17, 2016 (f) August 8–9, 2016 and (g) October 13–14, 2016 image pairs.

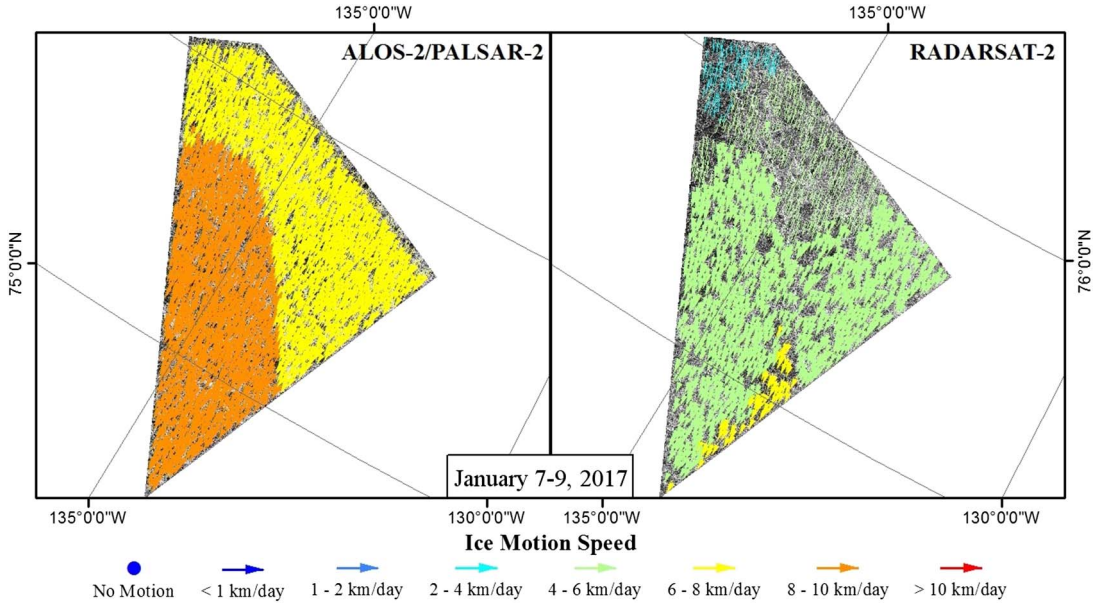

Fig. 7. Spatial distribution of L-band (left) and C-band (right) sea ice motion speeds over dry first-year ice for January 7–9, 2017 image pairs.

to C-band is observed (Fig. 4a). However, cross-correlations are higher for L-band at 0.482 compared to C-band at 0.329 (Fig. 6a; Table 2) because of more texture information in L-band within MYI floes which is clearly evident in Fig. 5a.

For the September 2010 image pairs, which are also representative of dry MYI conditions according to ASCAT (Fig. 3a), more vectors were also detected from the C-band pair compared to L-band, particularly apparent in the southwest and northwest regions of the image (Fig. 4b). Compared to the April image pairs, there is stronger convergence between the ice floes and this likely facilitated increased vector detection and a more continuous motion surface at L-band. Unlike during April however, L-band provided little, if any improvement in the cross-correlation coefficient (Fig. 6b; Table 2). It should be noted that although ASCAT σ° values in September are characteristic of dry MYI conditions, they are likely to differ from MYI conditions in the colder month of April. As a result, the texture differences between L- and C-band in the September image are not as strong compared to the April image pair and could account for similar cross-correlation coefficients (0.278) in September (Fig. 5b; Table 2).

4.2. Dry FYI

Fig. 7 illustrates the spatial distribution of sea ice motion for both C and L-band SAR during dry winter conditions over FYI in early January 2017 and more vectors were detected from L-band (2253) compared to C-band (1767) (Table 2). The spatial distribution of speed values is different because the start and end dates of the imagery are not exact and the faster ice drift was apparent from the L-band January 7–8 pair

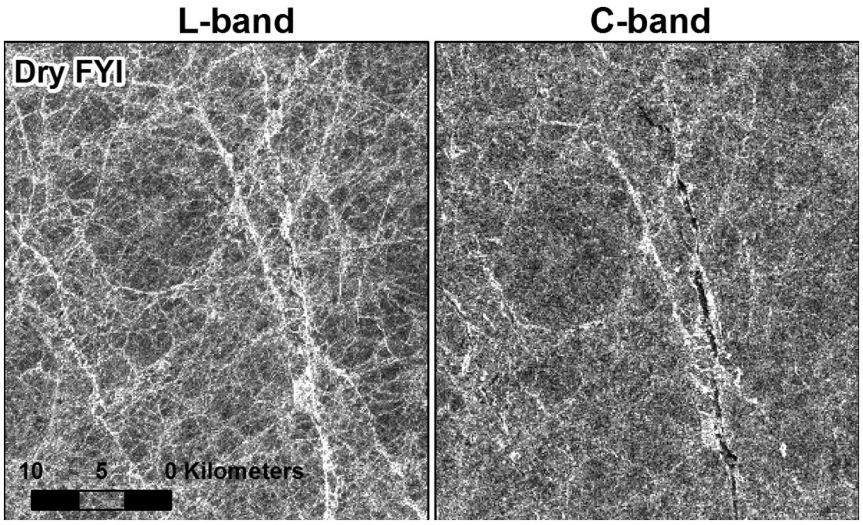

Fig. 8. Magnified images of L-band SAR (January 7, 2017) and C-band SAR (January 8, 2017) over dry first-year ice (FYI).

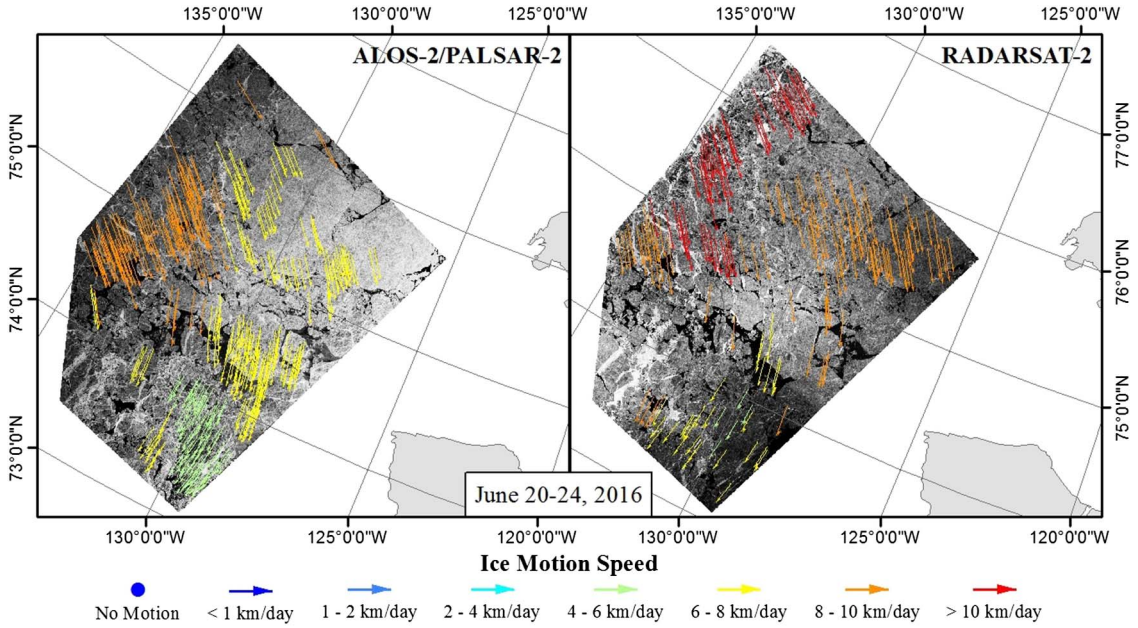

Fig. 9. Spatial distribution of L-band (left) and C-band (right) sea ice motion speeds over multi-year ice during the early melt period for June 20–24, 2016 image pairs.

compared to the C-band January 8–9 pair (Fig. 7; Table 2). More importantly, however, is that the cross-correlation coefficients associated with the L-band vectors are approximately twice as strong, indicating L-band SAR imagery provides both a qualitative and quantitative improvement over C-band when detecting sea ice motion over dry FYI (Table 2; Fig. 6c). Lehtiranta et al. (2015) also found higher cross-correlations with L-band compared to C-band in dry brackish ice conditions in the Baltic Sea. The large quantity of higher quality vectors detected by the ice tracking algorithm at L-band compared to C-band over dry FYI is likely the result of L-band being less sensitive to surface scattering (Winebrenner et al., 1989), but more sensitive to the physical and dielectric properties of deeper ice layers due to higher penetration of L-band compared to C-band. Evidence of this is illustrated in Fig. 8 whereby the higher contrast in L-band is more apparent compared to C-band and therefore, likely better feature matching.

4.3. Early and advanced MYI melt

During both the early and advanced melt periods, the improvement provided by the increased penetration depth of L-band SAR during the melt season (e.g. Onstott and Gogineni, 1985; Casey et al., 2016) facilitating increased sea ice motion vector detection is clearly evident (Figs. 9, 10). In all cases, the stronger contrast exhibited by L-band due to increased penetration within the ice compared to C-band is clearly apparent and this helps to facilitate improved feature identification (Fig. 11). Focusing on the early melt period case (June 20–24, 2016), the spatial distribution of sea ice in C- and L-band SAR is relatively similar for both bands (Fig. 9) but more vectors with stronger cross-correlations were associated with L-band compared to C-band with values of 3402 (0.198) and 2585 (0.182), respectively (Table 2; Fig. 6d). For all advanced melt image pair cases, the spatial distribution of the detected vectors is also similar (Fig. 10) but almost twice as many vectors were detected at L-band compared to C-band (Table 2). Despite the presence of more vectors for L-band there was almost no improvement of the cross-correlation coefficient compared to C-band during July (Table 2; Fig. 6e). The situation is slightly different in August where L-band continues to detect more motion vectors compared to C-band, and also provides stronger cross-correlations (Table 2; Fig. 6f). We suggest there is less surface water together with less absorptive wet snow in August compared to the July period as evident

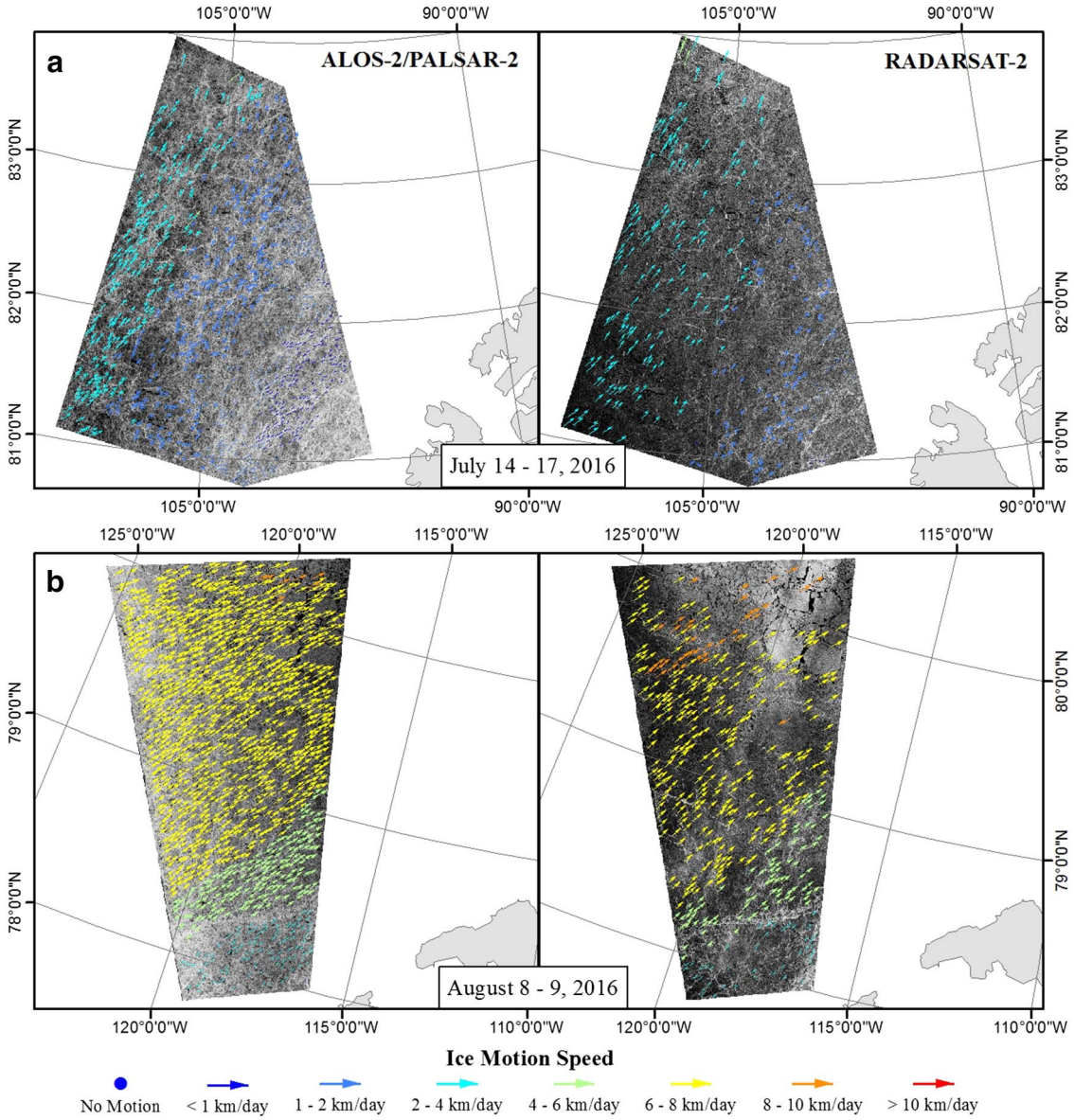

Fig. 10. Spatial distribution of L-band (left) and C-band (right) sea ice motion speeds over multi-year ice during the advanced melt period for (a) July 14–17, 2016 image pairs and (b) August 8–9, 2016 image pairs.

from brighter tone in Fig. 11c which favours the increased penetration of L-band resulting in increased vector identification with higher confidence.

It should be noted that the improvement in both the quality and number of detected vectors over MYI during the early melt period in L-band versus C-band SAR is not as substantial compared to the more advanced melt period (Table 2). For instance, during early melt period ~24% more vectors are detected at L-band but during the advanced melt during the number increases to between 34–48% together with stronger cross-correlations (Table 2). At the early melt stage for the June image pairs, the image quality of C-band has yet to experience the washed out homogeneity characteristics during the later stages of melt (Fig. 11a). As a result, there is likely minimal water content in the snow and/or at the snow-ice interface to appreciably reduce the penetration depth of C-band, resulting in similar feature detection compared to L-band. Overall, the ability of L-band SAR to provide improved sea ice discrimination during the melt season as compared to C-band SAR is consistent with suggestions from previous studies (Dierking, 2010; Casey et al., 2016).

4.4. New and grey white ice

Over new and grey white ice types, L-band also provides a better estimation of sea ice motion compared to C-band. The spatial distribution of detected sea ice motion for a region of new ice in the Beaufort Sea is shown in Fig. 12; considerably more vectors were detected for L-band compared to C-band, at 2971 and 371, respectively (Table 2). The cross-correlation coefficients are also considerably stronger for L-band (0.353) compared to C-band (0.228) (Fig. 6g; Table 2). The improvement of L-band over C-band for ice motion estimation during ice formation is likely because L-band is less sensitive to surface roughness during ice formation (Dierking and Busche, 2006), but more sensitive to the physical properties of the entire ice layer and the ice-water rough interface, which leads to a richer texture in L-band images which is evident in Fig. 13. Johansson et al. (2017) also suggested the later process when comparing L-band to C-band SAR co-polarization ratios. We note that the smaller number of ice motion vectors derived from the C-band image pair compared to the L-band image pair is not associated with a shorter time interval separating the C-band images (13h) compared to the time interval separating the L-

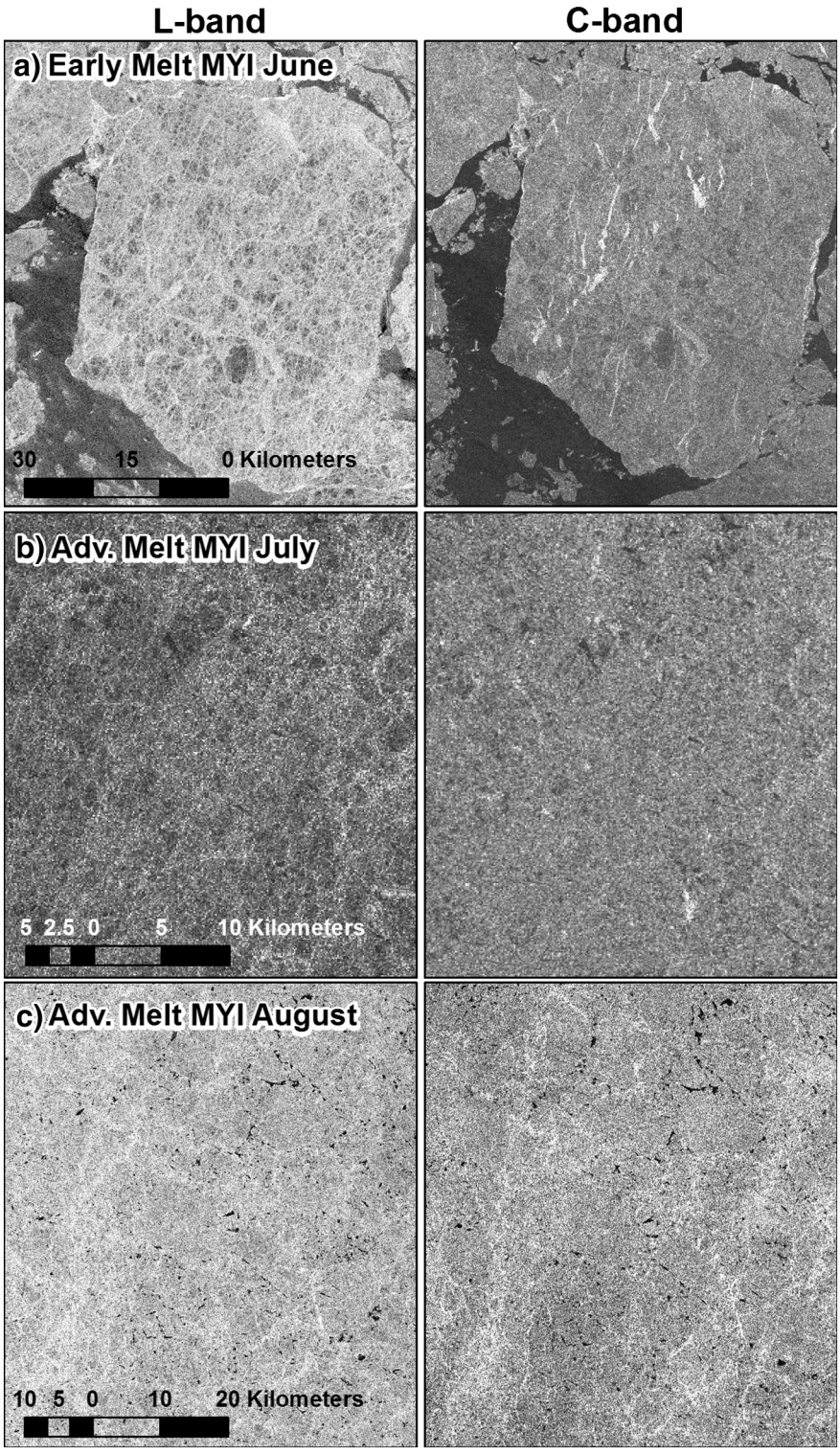

Fig. 11. Magnified images of L- and C-band SAR over multi-year ice (MYI) during (a) early melt conditions on June 20, 2016, (b) advanced melt conditions on July 14, 2016 and (c) advanced melt conditions on August 8, 2016.

band images (24 h). In fact, a larger number of vectors is expected to be derived from a SAR image pair with a shorter separation time compared to a SAR image pair with a larger separation time encompassing that shorter time interval.

This October ice case differs from our April case where C-band provided more ice information than L-band because the ice in October was thicker than the very thin ice between the MYI floes in April, which formed from very recent divergent ice motion. Arkett et al. (2008) reported that L-band imagery can better identify thinner ice compared to C-band and in our new/grey white ice case, C-band feature detection was certainly less compared to L-band. This could have also been further impeded by strong wind conditions producing strong surface scattering at C-band (i.e. sea ice motion was greater than 10 km per day for all vectors). Subsequent splashing of water on the ice surface as well as potential presence of frost flowers producing enhanced surface scattering at C-band are additional possible contributing factors.

5. Conclusions

Previous research has suggested that L-band SAR could theoretically

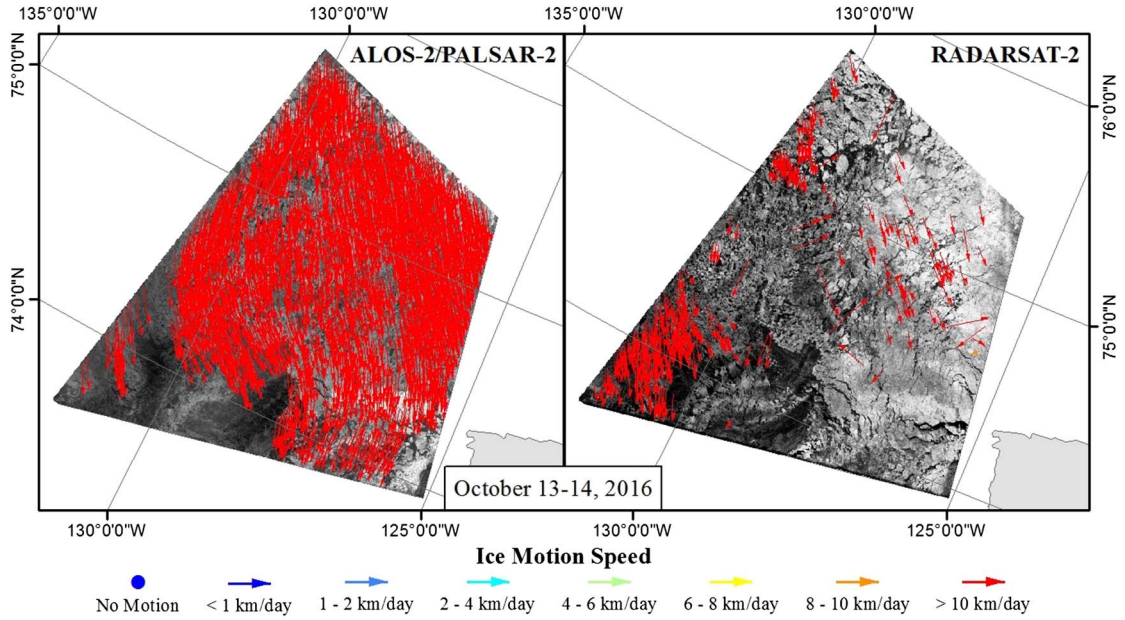

Fig. 12. Spatial distribution of L-band (left) and C-band (right) sea ice motion speeds over new and grey white ice during the ice formation period for the October 13–14, 2016 image pairs.

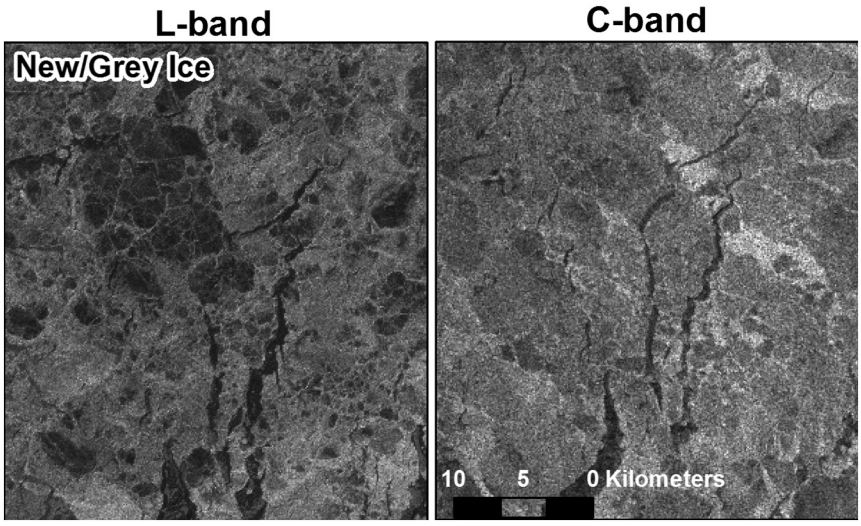

Fig. 13. Magnified images of L- and C-band SAR over new and grey white ice on October 14, 2016.

provide improved estimates of sea ice motion particularly during the melt season (Dierking and Busche, 2006; Dierking, 2010) but very few studies have actually quantified this application (e.g. Lehtiranta et al., 2015). We analyzed sea ice motion detection from 9 sets of near coincident C- and L-band SAR imagery co-located in the Canadian Arctic over a variety of sea ice types and different thermodynamic states during 2010, 2016 and 2017. L-band SAR imagery from PALSAR-1 and PALSAR-2 was able to detect more sea ice motion vectors compared to RADARSAT-2 for multi-year ice during the melt season, dry first-year ice and new/grey white ice during freeze-up. In addition to providing more motion vectors, the cross-correlation coefficients in almost all cases were stronger for L-band SAR compared to C-band SAR. These results indicate that during the melt and freeze-up seasons, L-band SAR could find more operational value compared to C-band SAR. Similarly, for sea ice processes applications L-band SAR would provide more representative quantitative sea ice motion information.

L-band SAR detected ice motion over dry MYI during April was not as spatially representative compared to C-band. This is because the ice tracking algorithm had difficulty resolving very thin ice between the MYI floe boundaries for the L-band SAR images. The situation was improved in September because of more closely packed MYI but the cross-correlation coefficients were lower than reported in April. Based on this, differences in ice motion derived from C- and L-band SAR over dry MYI may require further investigation. For instance, we found that the quantity and quality of the ice motion vectors between MYI floes may vary depending on how recently the new ice forms between floes associated with convergent or divergent ice motion.

Overall, L-band SAR imagery from PALSAR-1 and PALSAR-2 shows promising results for detecting sea ice motion during shoulder seasons which is more difficult from C-band SAR. Johansson et al. (2017) also recently demonstrated the value of L-band SAR for identifying ice types that are difficult using C-band SAR. Given that the Arctic sea ice continues to transition from a MYI to FYI icescape (e.g. Maslanik et al., 2011) which includes longer melt season lengths (e.g. Stroeve et al., 2014), the benefits of L-band SAR imagery are perhaps more relevant in today's climate compared to decades ago. Indeed ship traffic in the Canadian Arctic is increasing (e.g. Pizzolato et al., 2016) and it is imperative that operational ice services are able to identify and predict the location and trajectory of MYI in order to prevent marine disasters. With the current availability of PALSAR-2 and the eventual availability

of L-band SAR imagery from NASA-ISRO SAR Mission (NISAR) (Rosen et al., 2016) we will be able to continue to provide improved estimates of sea ice motion in upcoming years.

Acknowledgements

PALSAR-2 images were provided by Japan Aerospace Exploration Agency (JAXA) under the 4th Research Announcement program (PI NO. 1202, S. Howell) and through a joint sharing agreement between Canadian Space Agency (CSA) and JAXA. PALSAR-1 images were provided by the Alaska Satellite Facility (https://vertex.daac.asf.alaska.edu/). RADARSAT-2 data and products © MacDonald, Dettwiler and Associates Ltd. (2013) – All Rights Reserved. RADARSAT is an official mark of the Canadian Space Agency. RADARSAT-2 imagery are available for a fee from the National Earth Observation Data Framework Catalog (https://neodf.nrcan.gc.ca). ASCAT SIR data were provided by Scatterometer Climate Record Pathfinder at Brigham Young University courtesy of David G. Long (http://www.scp.byu.edu/). We would like to thank the anonymous reviewers for providing very useful comments which helped improved the quality of this manuscript.

References

Arkett, M., Flett, D., De Abreu, R., Clemente-Colon, P., Woods, J., Melchior, B., 2008. Evaluating ALOS-PALSAR for ice monitoring-what can L-band do for the North American ice service? In: Geoscience and Remote Sensing Symposium, IGARSS 2008, IEEE International. 5 (V–188).

Barber, D.G., Reddan, S.P., LeDrew, E.F., 1995. Statistical characterization of the geophysical and electrical properties of snow on landfast first-year sea ice. J. Geophys. Res. Oceans (1978–2012) 100 (C2), 2673–2686.

Beaven, S.G., Gogineni, S.P., 1994. Shipborne radar backscatter measurements from Arctic sea ice during the fall freeze-up. Remote Sens. Rev. 9 (1–2), 3–25. http://dx.doi.org/10.1080/02757259409532211.

Canadian Ice Service, 2007. Regional charts: History, accuracy, and caveats, Arch. Doc. Ser. 1, Ottawa. Available at. http://ice.ec.gc.ca/IA_DOC/cisads_no_001_e.pdf.

Canadian Ice Service, 2011. Sea ice climatic Atlas: Northern Canadian waters 1981–2010, 995 pp., Ottawa. Available at. http://www.ec.gc.ca/glacesice/default.asp?lang5En&n54B35305B-1.

Casey, J.A., Howell, S.E.L., Tivy, A., Haas, C., 2016. Separability of sea ice types from wide swath C- and L-band synthetic aperture radar imagery acquired during the melt season. Remote Sens. Environ. 174, 314–328. http://dx.doi.org/10.1016/j.rse.2015.12.021.

Comiso, J.C., 2012. Large decadal decline of the Arctic multiyear ice cover. J. Clim. 25, 1176–1193. http://dx.doi.org/10.1175/JCLI-D-11–00113.1.

Dierking, W., 2010. Mapping of different sea ice regimes using images from Sentinel-1 and ALOS synthetic aperture radar. IEEE Trans. Geosci. Remote Sens. 48 (3), 1045–1058. http://dx.doi.org/10.1109/TGRS.2009.2031806.

Dierking, W., Busche, T., 2006. Sea ice monitoring by L-band SAR: an assessment based on literature and comparisons of JERS-1 and ERS-1 imagery. IEEE Trans. Geosci. Remote Sens. 44 (4), 957–970. http://dx.doi.org/10.1109/TGRS.2005.861745.

Early, D.S., Long, D.G., 2001. Image reconstruction and enhanced resolution imaging from irregular samples. IEEE Trans. Geosci. Remote Sens. 39 (2), 291–302. http://dx.doi.org/10.1109/36.905237.

Howell, S.E.L., Wohlleben, T., Dabboor, M., Derksen, C., Komarov, A., Pizzolato, L., 2013. Recent changes in the exchange of sea ice between the Arctic Ocean and the Canadian Arctic Archipelago. J. Geophys. Res. Oceans 118, 3595–3607. http://dx.doi.org/10.1002/jgrc.20265.

Howell, S.E.L., Brady, M., Derksen, C., Kelly, R.E.J., 2016. Recent changes in sea ice area flux through the Beaufort Sea during the summer. J. Geophys. Res. Oceans 121, 2659–2672. http://dx.doi.org/10.1002/2015JC011464.

Hwang, B., 2013. Inter-comparison of satellite sea ice motion with drifting buoy data. Int. J. Remote Sens. 34 (24), 8741–8763. http://dx.doi.org/10.1080/01431161.2013.848309.

Johansson, A.M., King, J.A., Doulgeris, A.P., Gerland, S., Singha, S., Spreen, G., Busche, T., 2017. Combined observations of Arctic sea ice with near-coincident colocated X-band, C-band, and L-band SAR satellite remote sensing and helicopter-borne measurements. J. Geophys. Res. Oceans 122, 669–691. http://dx.doi.org/10.1002/2016JC012273.

Karvonen, J., Simila, M., Lehtiranta, J., 2007. SAR-based estimation of the Baltic sea ice motion. In: Proceedings of the International Geoscience and Remote Sensing Symposium 2007 (IGARSS-07). IEEE, Barcelona, Spain, pp. 2605–2608.

Komarov, A.S., Barber, D.G., 2014. Sea ice motion tracking from sequential dual-polarization RADARSAT-2 images. IEEE Trans. Geosci. Remote Sens. 52 (1), 121–136. http://dx.doi.org/10.1109/TGRS.2012.2236845.

Kwok, R., Cunningham, G.F., 2010. Contribution of melt in the Beaufort Sea to the decline in Arctic multiyear sea ice coverage: 1993–2009. Geophys. Res. Lett. 37, L20501. http://dx.doi.org/10.1029/2010GL044678.

Kwok, R., Cunningham, G.F., 2015. Variability of Arctic sea ice thickness and volume from CryoSat-2. Philos. Trans. R. Soc., A 373, 20140157. http://dx.doi.org/10.1098/rsta.2014.0157.

Kwok, R., Curlander, J., McConnell, R., Pang, S., 1990. An ice-motion tracking system at the Alaska SAR facility. IEEE J. Ocean. Eng. 15 (1), 44–54.

Kwok, R., Pedersen, L.T., Gudmandsen, P., Pang, S.S., 2010. Large sea ice outflow into the Nares Strait in 2007. Geophys. Res. Lett. 37, L03502. http://dx.doi.org/10.1029/2009GL041872.

Kwok, R., Spreen, G., Pang, S., 2013. Arctic sea ice circulation and drift speed: decadal trends and ocean currents. J. Geophys. Res. Oceans 118. http://dx.doi.org/10.1002/jgrc.20191.

Lehtiranta, J., Siiriä, S., Karvonen, J., 2015. Comparing C- and L-band SAR images for sea ice motion estimation. Cryosphere 9, 357–366. http://dx.doi.org/10.5194/tc-9-357-2015.

Lindsley, R.D., Long, D.G., 2010. Standard BYU ASCAT land/ice image products. In: MERS Technical Report # MERS 10-02, Available at. http://www.scp.byu.edu/docs/pdf/MERS1002.pdf.

Livingstone, C.E., Singh, K.P., Gray, A.L., 1987. Seasonal and regional variations of active/passive microwave signatures of sea ice. IEEE Trans. Geosci. Remote Sens. GE-25 (2), 159–173. http://dx.doi.org/10.1109/TGRS.1987.289815.

Mahmud, M.S., Howell, S.E.L., Geldsetzer, T., Yackel, J., 2016. Detection of melt onset over the northern Canadian Arctic Archipelago sea ice from RADARSAT, 1997–2014. Remote Sens. Environ. 178, 59–69. http://dx.doi.org/10.1016/j.rse.2016.03.003.

Maslanik, J., Stroeve, J., Fowler, C., Emery, W., 2011. Distribution and trends in Arctic sea ice age through spring 2011. Geophys. Res. Lett. 38, L13502. http://dx.doi.org/10.1029/2011GL047735.

McConnell, R., Kwok, R., Curlander, J., Pang, S., Kobe, W., 1991. Ψ-S correlation and dynamic time warping: two methods for tracking ice floes in SAR images. IEEE Trans. Geosci. Remote Sens. 29 (6), 1004–1012.

Melia, N., Haines, K., Hawkins, E., 2016. Sea ice decline and 21st century trans-Arctic shipping routes. Geophys. Res. Lett. 43, 9720–9728. http://dx.doi.org/10.1002/2016GL069315.

Mortin, J., Howell, S.E.L., Wang, L., Derksen, D., Svensson, G., Graversen, R.G., Schrøder, T.M., 2014. Extending the QuikSCAT record of seasonal melt–freeze transitions over Arctic sea ice using ASCAT. Remote Sens. Environ. 141, 214–230. http://dx.doi.org/10.1016/j.rse.2013.11.004.

Olason, E., Notz, D., 2014. Drivers of variability in Arctic sea-ice drift speed. J. Geophys. Res. Oceans 119, 5755–5775. http://dx.doi.org/10.1002/2014JC009897.

Onstott, R.G., Gogineni, S.P., 1985. Active microwave measurements of Arctic sea ice under summer conditions. J. Geophys. Res. 90 (C3), 5035–5044. http://dx.doi.org/10.1029/JC090iC03p05035.

Onstott, R.G., Grenfell, T.C., Matzler, C., Luther, C.A., Svendsen, E.A., 1987. Evolution of microwave sea ice signatures during early summer and midsummer in the marginal ice zone. J. Geophys. Res. 92 (C7), 6825–6835. http://dx.doi.org/10.1029/JC092iC07p06825.

Petty, A.A., Hutchings, J.K., Richter-Menge, J.A., Tschudi, M.A., 2016. Sea ice circulation around the Beaufort Gyre: the changing role of wind forcing and the sea ice state. J. Geophys. Res. Oceans 121, 3278–3296. http://dx.doi.org/10.1002/2015JC010903.

Pizzolato, L., Howell, S.E.L., Dawson, J., Laliberté, F., Copland, L., 2016. The influence of declining sea ice on shipping activity in the Canadian Arctic. Geophys. Res. Lett. 43. http://dx.doi.org/10.1002/2016GL071489.

Rampal, P., Weiss, J., Marsan, D., 2009. Positive trend in the mean speed and deformation rate of Arctic sea ice, 1979–2007. J. Geophys. Res. 114, C05013. http://dx.doi.org/10.1029/2008JC005066.

Rosen, P., et al., 2016. An update on the NASA-ISRO dual-frequency DBF SAR (NISAR) mission. In: Proceedings From 2016 IEEE International Geoscience and Remote Sensing Symposium (IGARSS), (10.1109/IGARSS.2016.772954310.1109/IGARSS.2016.7729543).

Scharien, R.K., Hochheim, K., Landy, J., Barber, D.G., 2014. First-year sea ice melt pond fraction estimation from dual-polarisation C-band SAR — part 2: scaling in situ to Radarsat-2. Cryosphere 8, 2163–2176. http://dx.doi.org/10.5194/tc-8-2163-2014.

Smith, L.C., Stephenson, S.R., 2013. New trans-Arctic shipping routes navigable by midcentury. Proc. Natl. Acad. Sci. U. S. A. (13), 4871–4872. http://dx.doi.org/10.1073/pnas.1214212110.

Spreen, G., Kwok, R., Menemenlis, D., 2011. Trends in Arctic sea ice drift and role of wind forcing: 1992–2009. Geophys. Res. Lett. 38 (19), L19 501.

Stroeve, J.C., Serreze, M.C., Holland, M.M., Kay, J.E., Maslanik, J., Barrett, A.P., 2012. The Arctic's rapidly shrinking sea ice cover: a research synthesis. Clim. Chang. 110 (3–4), 1005–1027. http://dx.doi.org/10.1007/s10584-011-0101-1.

Stroeve, J.C., Markus, T., Boisvert, L., Miller, J., Barrett, A., 2014. Changes in Arctic melt season and implications for sea ice loss. Geophys. Res. Lett. 41 (4), 1216–1225. http://dx.doi.org/10.1002/2013GL058951.

Thomas, M., Geiger, C., Kambhamettu, C., 2008. High resolution (400 m) motion characterization of sea ice using ERS-1 SAR imagery. J. Cold Reg. Sci. Technol. 52, 207–223.

Wang, L., Wolken, G.J., Sharp, M.J., Howell, S.E.L., Derksen, C., Brown, R.D., Markus, T., Cole, J., 2011. Integrated pan-Arctic melt onset detection from satellite active and passive microwave measurements, 2000–2009. J. Geophys. Res. 116, D22103. http://dx.doi.org/10.1029/2011JD016256.

Winebrenner, D.P., Tsang, L., Wen, B., West, R., 1989. Sea-ice characterization measurements needed for testing of microwave remote sensing models. IEEE J. Ocean. Eng. 14 (2), 149–158. http://dx.doi.org/10.1109/48.16828.

Winebrenner, D.P., Nelson, E.D., Colony, R., West, R.D., 1994. Observation of melt onset on multiyear Arctic sea ice using ERS 1 synthetic aperture radar. J. Geophys. Res. 99 (C11), 22425–22441. http://dx.doi.org/10.1029/94JC01268.

Wohlleben, T., Howell, S.E.L., Agnew, T., Komarov, A., 2013. Sea ice motion and flux within the Prince Gustaf Adolf Sea, Queen Elizabeth Islands, Canada during 2010. Atmosphere-Ocean 51, 1–17. http://dx.doi.org/10.1080/07055900.2012.750232.

Yackel, J.J., Barber, D.G., Papakyriakou, T.N., Breneman, C., 2007. First-year sea ice spring melt transitions in the Canadian Arctic Archipelago from time-series synthetic aperture radar data, 1992–2002. Hydrol. Process. 21 (2), 253–265.